1

An alternative binding mode of IGHV3-53 antibodies

to the SARS-CoV-2 receptor binding domain

4

5

Nicholas C. Wu[1,*], Meng Yuan[1,*], Hejun Liu[1,*], Chang-Chun D. Lee[1], Xueyong Zhu[1],

Sandhya Bangaru[1], Jonathan L. Torres[1], Tom G. Caniels[2], Philip J.M. Brouwer[2], Marit J.

van Gils[2], Rogier W. Sanders[2,3], Andrew B. Ward[1,4,5], Ian A. Wilson[1,4,5,6,§]

9

10

[1] Department of Integrative Structural and Computational Biology, The Scripps Research

Institute, La Jolla, CA 92037, USA

[2] Department of Medical Microbiology, Amsterdam UMC, University of Amsterdam,

Amsterdam Infection & Immunity Institute, 1105AZ Amsterdam, the Netherlands

[3] Department of Microbiology and Immunology, Weill Medical College of Cornell

University, New York, NY 10021, USA

[4] IAVI Neutralizing Antibody Center, The Scripps Research Institute, La Jolla, CA 92037,

USA

[5] Consortium for HIV/AIDS Vaccine Development (CHAVD), The Scripps Research

Institute, La Jolla, CA 92037, USA

[6] The Skaggs Institute for Chemical Biology, The Scripps Research Institute, La Jolla,

CA, 92037, USA

* These authors contributed equally to this work

§ Correspondence: wilson@scripps.edu (I.A.W.)

ABSTRACT

IGHV3-53-encoded neutralizing antibodies are commonly elicited during SARS-CoV-2 infection and target the receptor-binding domain (RBD) of the spike (S) protein. Such IGHV3-53 antibodies generally have a short CDR H3 due to structural constraints in binding the RBD (mode A). However, a small subset of IGHV3-53 antibodies to the RBD contain a longer CDR H3. Crystal structures of two IGHV3-53 neutralizing antibodies here demonstrate that a longer CDR H3 can be accommodated in a different binding mode (mode B). These two classes of IGHV3-53 antibodies both target the ACE2 receptor binding site, but with very different angles of approach and molecular interactions. Overall, these findings emphasize the versatility of IGHV3-53 in this common antibody response to SARS-CoV-2, where conserved IGHV3-53 germline-encoded features can be combined with very different CDR H3 lengths and light chains for SARS-CoV-2 RBD recognition and virus neutralization.

38 **INTRODUCTION**

39 Development of an effective vaccine against severe acute respiratory syndrome

40 coronavirus 2 (SARS-CoV-2) is perhaps the most exigent health-related priority due to the

41 ongoing COVID-19 pandemic. However, the molecular and functional understanding of

42 the antibody response to SARS-CoV-2 infection and vaccination is still somewhat limited,

43 but is critical for vaccine assessment and redesign. Most SARS-CoV-2 antibodies that

44 target the receptor-binding domain (RBD) on the spike (S) protein appear to be

45 neutralizing (Brouwer et al., 2020; Cao et al., 2020; Robbiani et al., 2020; Rogers et al.,

46 2020; Zost et al., 2020) and the most intuitive mechanism of neutralization is that they

47 block binding of the host receptor angiotensin-converting enzyme 2 (ACE2).

48

49 To date, several structures of antibodies that target the ACE2-binding site on RBD have

50 been determined (Cao et al., 2020; Ju et al., 2020; Shi et al., 2020), including some that

51 are encoded by the IGHV3-53 gene (Barnes et al., 2020; Brouwer et al., 2020; Wu et al.,

52 2020; Yuan et al., 2020a). Our previous study demonstrated that antibodies encoded by

53 the IGHV3-53 gene utilize germline-encoded residues to engage the ACE2-binding site

54 on the RBD, accounting for their frequency in shared antibody responses in SARS-CoV-

55 2 patients (Yuan et al., 2020a). Due to structural constraints in their mode of binding

56 through interaction with the germline-encoded heavy chain complementarity determining

57 regions (CDR) H1 and H2, a short CDR H3 (length of ≤10 amino acids, Kabat numbering)

58 is also a molecular signature of these IGHV3-53 antibodies (Barnes et al., 2020; Yuan et

59 al., 2020a). Nevertheless, a small subset (around 10%) of RBD-targeting IGHV3-53

60 antibodies have much longer CDR H3s (15 amino acids or longer) (Barnes et al., 2020;

61 Yuan et al., 2020a). As it was not apparent how such IGHV3-53 antibodies could retain

62 the same binding mode and fit their longer CDR H3 into a highly restricted pocket in the

63 RBD (Yuan et al., 2020a), we aimed to resolve this conundrum.

3

64

RESULTS

Two RBD-targeting IGHV3-53 antibodies with different binding modes

We determined crystal structures of two IGHV3-53 neutralizing antibodies, COVA2-04 and COVA2-39 (Brouwer et al., 2020), with different CDR H3 lengths in complex with SARS-CoV-2 RBD to 2.35 and 1.72 Å resolutions, respectively (Figure 1A and Table S1). Both antibodies were derived from a convalescent donor from Amsterdam and potently neutralize SARS-CoV-2 virus (Brouwer et al., 2020). Similar to typical RBD-targeting IGHV3-53 antibodies (Barnes et al., 2020; Wu et al., 2020; Yuan et al., 2020a), COVA2-04 has a relatively short CDR H3 of 10 amino acids, whereas COVA2-39 CDR H3 is 15 amino acids (Kabat numbering, Figure S1A). COVA2-04 has only two somatic amino-acid substitutions in the heavy chain and one in the light chain, which is encoded by IGKV3-20 (Figure S1B). COVA2-39 has three somatic mutations in the heavy chain and one in the light chain, which is encoded by IGLV2-23 (Figure S1C).

COVA2-04 and COVA2-39 both bind to the ACE2-binding site on RBD, which is consistent with previous competition assays (Brouwer et al., 2020). Nonetheless, their angles of approach and binding modes are very different (Figure 1A-C). COVA2-04 mainly uses the light chain to interact with the flat surface of the ACE2-binding site and the heavy chain with the RBD ridge, whereas COVA2-39 mainly uses the heavy chain to interact with the flat surface and both heavy and light chains with the ridge (Figure 1B, Figure 2A-B and Table S2). In addition, COVA2-04 binds to the side of the ridge, whereas COVA2-39 binds at its tip (Figure 1B). The binding mode of COVA2-04 is very similar to previously characterized IGHV3-53 antibodies with a short CDR H3, including CC12.1, CC12.3, B38, and C105 (Barnes et al., 2020; Wu et al., 2020; Yuan et al., 2020a) (binding mode A, Figure 1C). In contrast, binding mode (mode B) of COVA2-39 is quite different and its Fab

4

90   is rotated 180° along its long axis relative to COVA2-04, thereby swapping the relative

91   orientation of the light and heavy chains, resulting in completely different molecular

92   interactions.

93

94   **Both binding modes are dominated by heavy chain**

95   Structural modeling shows that both COVA2-04 and COVA2-39 can only bind to the RBD

96   when it is in the "up" conformation on the trimeric S protein (Figure S2) (Walls et al., 2020;

97   Wrapp et al., 2020). This finding is consistent with previous low-resolution, negative-stain

98   electron microscopy analysis, which also indicated that these antibodies have different

99   angles of approach (Brouwer et al., 2020). Despite these differences, interactions of

100   COVA2-04 and COVA2-39 with the RBD are both dominated by the heavy chain. For

101   COVA2-04, the buried surface areas (BSA) of the heavy and light chains are 798 Å^2 and

102   360 Å^2, respectively, compared to 576 Å^2 and 128 Å^2 for COVA2-39. However, this BSA

103   difference does not translate into a corresponding difference in Fab binding affinity.

104   Specifically, the dissociation constants (K_d) for COVA2-04 and COVA2-39 to insect cell-

105   expressed RBD are 40 nM and 21 nM, respectively (Figure 1D). COVA2-04 exhibits slow-

106   on/slow-off kinetics, whereas COVA2-39 has fast-on/fast-off kinetics. Despite the faster

107   off-rate, similar K_d and lower BSA, COVA2-39 IgG is more potent than COVA2-04 in

108   neutralizing SARS-CoV-2 (IC_{50}s of 0.036 and 0.22 μg/ml, respectively, in a pseudovirus

109   assay, and 0.054 and 2.5 μg/ml in an authentic virus assay (Brouwer et al., 2020)).

110

111   Compared to COVA2-04, the COVA2-39 epitope has less overlap with the ACE2-binding

112   site. Among 17 ACE2-binding residues on the RBD (Lan et al., 2020), 16 are within the

113   epitope of COVA2-04 and 11 within the epitope of COVA2-39 (Figure 2A-C). The

114   difference in angles of approach and apparent avidity of the IgG interaction in the context

115   of the spike trimer appear to allow COVA2-39 attain higher neutralization potency, similar

5

116   to avidity effects for IgG of some antibodies to influenza hemagglutinin RBD (Ekiert et al.,

117   2012; Lee et al., 2014). Indeed, the K_d of IgG to mammalian cell-expressed SARS-CoV-2

118   spike protein is 2.3 nM for COVA2-04 and 0.1 nM for COVA2-39 (Brouwer et al., 2020),

119   which represents a 20-fold difference in apparent IgG binding avidity that may also result

120   from the higher local Fab concentration and rebinding of IgG to the spike protein on both

121   the sensor in the binding experiment and on viral surface.

122

123   **Both binding modes involve similar motifs**

124   Previously, we have described the germline-encoded features of IGHV3-53, including an

125    $_{32}NY_{33}$ motif in CDR H1 and an $_{53}SGGS_{56}$ motif in CDR H2, which facilitate interaction with

126   the ACE2-binding site of SARS-CoV-2 RBD in binding mode A (Yuan et al., 2020a). These

127   motifs are also important for COVA2-04 engagement of the RBD in a similar manner to

128   other IGHV3-53 antibodies in binding mode A (Figure 3A-B) (Yuan et al., 2020a).

129   Interestingly, some of these germline-encoded residues are also involved in binding of

130   COVA2-39 (mode B), but to a different location and, hence, to different residues on the

131   RBD. V_H Y33 of the $_{32}NY_{33}$ motif is retained and forms a π−π stacking interaction between

132   its aromatic ring with the aromatic side chain of Y489 (Figure 3C). Although V_H N32 in

133   COVA2-39 does not interact with the RBD, both its side chain and main chain participate

134   in a 3_{10} turn to stabilize the CDR H1 backbone (Figure 3C), similar to that observed with

135   COVA2-04 and other IGHV3-53 antibodies (Figure 3A) (Yuan et al., 2020a). The $_{53}SGGS_{56}$

136   is somatically mutated to $_{53}TGGT_{56}$ in COVA2-39, which would appear to be a

137   conservative substitution. Similar to the $_{53}SGGS_{56}$ motif in binding mode A (Figure 3B),

138   the $_{53}TGGT_{56}$ motif in COVA2-39 also forms an extensive hydrogen-bond (H-bond)

139   network (Figure 3D), but to a different region of SARS-CoV-2 RBD (Figure S3). The

140    $_{53}TGGT_{56}$ motif in COVA2-39 extensively H-bonds with RBD E484 through the side chains

141   of V_H T53 and V_H T56 (water-mediated H-bond), as well as the backbone amides of V_H

6

142   T53, V_H G55, and V_H T56 (Figure 3D). The side chains of V_H T53 and V_H T56 also

143   participate in additional water-mediated H-bonds with backbone carbonyls and amides of

144   the RBD. Nevertheless, despite the similarity between Ser and Thr in size and ability to

145   form similar H-bonds with their side-chain hydroxyl, reverting the $_{53}TGGT_{56}$ motif in

146   COVA2-39 to the germline-encoded $_{53}SGGS_{56}$ motif decreased its K_d to SARS-CoV-2

147   RBD by at least 50-fold (Figure 1D and Figure S4A). The increased binding for $_{53}TGGT_{56}$

148   is likely due to the methyl groups in V_H T53 and T56, which make additional van der Waals

149   interactions (Figure S4B).

150

151   Similar to the $_{53}SGGS_{56}$ motif, $_{53}TGGT_{56}$ in COVA2-39 takes part in a type I beta turn along

152   with V_H Y52, which is the first residue (i) in the turn (YTGG). The partial positive dipole

153   from the aligned amides at the amino-end of the turn forms a charged interaction with the

154   RBD E484 carboxyl group. Moreover, V_H Y52 is an important residue for binding SARS-

155   CoV-2 RBD in binding mode B, but not in binding mode A (Figure 3E). V_H Y52 of COVA2-

156   39 forms a π−π interaction with backbone peptide bond between RBD G485 and F486.

157   COVA2-39 also employs other IGHV3-53 germline-encoded residues for interaction with

158   the RBD, including V_H S30, V_H Y58, V_H N73, and V_H S74 (Figure S4C-D). Overall, these

159   findings demonstrate that the germline-encoded features of IGHV3-53 are conducive for

160   interaction with different regions of the ACE2-binding site on the RBD that involve different

161   approach angles (i.e. binding modes A and B) in the context of different CDR H3 lengths.

162

163   **Binding mode B has less structural constraints on CDR H3 length**

164   Next we aimed to understand the relationship between CDR H3 length and the two

165   different binding modes. Consistent with previous structures of IGHV3-53 antibodies that

166   target the RBD in binding mode A (Barnes et al., 2020; Wu et al., 2020; Yuan et al., 2020a),

167   CDR H3 of COVA2-04 is highly buried by the RBD and the light chain (Figure 4A). This

7

168   observation substantiates the notion that IGHV3-53 in binding mode A has strong

169   structural constraints on CDR H3 length. In contrast, in binding mode B, the longer CDR

170   H3 of COVA2-39 is largely solvent exposed (Figure 4B). This observation explains why

171   IGHV3-53 can accommodate a longer CDR H3 in binding mode B (COVA2-39) compared

172   to mode A (COVA2-04, CC12.1, CC12.3, B38, and C105). Interestingly, COVA2-39 CDR

173   H3 interacts with the RBD mostly through non-specific van der Waals interactions. Three

174   H-bonds are also made, two of which (one water-mediated) involve the CDR H3

175   backbone, whereas only one involves a side chain (V_H E100c) (Figure 4C). Thus,

176   interaction between CDR H3 of COVA2-39 and RBD is largely sequence non-specific and

177   simply accommodates its longer length. The CDR H3 sequences of IGHV3-53 antibodies

178   in binding mode A (COVA2-04, CC12.1, CC12.3, and B38) are also quite different (Wu et

179   al., 2020; Yuan et al., 2020a) (Figure 4D). As a result, while both binding modes A and B

180   do not have strong constraints on the actual CDR H3 sequences, structural constraints on

181   CDR H3 length is much stronger in binding mode A compared to mode B.

182

183   **Light chain of IGHV3-53 antibody is associated with CDR H3 length**

184   An important feature in COVA2-39 interaction with the RBD is its engagement of the

185   ACE2-binding ridge. Specifically, RBD F486 at the tip of the ridge is anchored in a pocket

186   formed by both heavy and light chains (Figure 5A). RBD F486 forms a π−π stacking

187   interaction with V_L Y91, which in turn is stabilized by a network of T-shaped π−π stacking

188   interactions involving V_H W47, V_H F100g, V_L Y30, and V_L W96 (Figure 5B, Figure S5). This

189   critical interaction with the ridge indicates that the light-chain identity is important for

190   binding mode B. In fact, the CDR H3 lengths of RBD-targeting IGHV3-53 antibodies seem

191   to depend on the light chain identity. For example, all known RBD-targeting IGHV3-53

192   antibodies that pair with IGKV1-9 (n = 20) and IGKV3-20 (n = 15) have a relatively short

193   CDR H3 (7 to 11 amino acids) (Figure 5C) (Brouwer et al., 2020; Cao et al., 2020; Ju et

8

194   al., 2020; Robbiani et al., 2020; Rogers et al., 2020; Wu et al., 2020). In contrast, all three

195   known RBD-targeting IGHV3-53 antibodies that pair with IGLV2-23, including COVA2-39,

196   have a CDR H3 of 14 amino acids or longer (Figure 5C). Therefore, despite the limited

197   sample size, there seems to be a relationship between the light chain identity of RBD-

198   targeting IGHV3-53 antibodies and CDR H3 length. This observation further supports a

199   role for light-chain identity, together with CDR H3 length, in determining the particular

200   binding mode of IGHV3-53 antibodies to SARS-CoV-2 RBD.

201

202   **DISCUSSION**

203   The additional binding mode identified here demonstrates that IGHV3-53 is even more

204   versatile than previously thought in SARS-CoV-2 RBD-targeting antibodies (Yuan et al.,

205   2020a). However, a remaining question is why binding mode A is more commonly seen

206   given the structural constraints for below average CDR H3 length, even for VH3-53

207   antibodies in general (Barnes et al., 2020; Wu et al., 2020; Yuan et al., 2020a). In mode

208   A, the germline sequences of CDR H1 and H2, along with a conserved residue in FR3,

209   seems to be the major determinant of binding without much involvement of specific

210   residues of CDR H3. In binding mode B, formation of the RBD ridge-anchoring pocket

211   involves both CDR H3 and L3 loops. In COVA2-39, the RBD ridge-anchoring pocket is

212   formed from V_H F100g in CDR H3 and V_L W96 in CDR L3 and generated during V(D)J

213   recombination. Thus, the probability of satisfying the molecular requirements to create the

214   RBD ridge-anchoring pocket (binding mode B) could be less than simply using the

215   unmutated germline sequence with no particular CDR H3 sequence requirements other

216   than length (binding mode A). Nonetheless, additional structures of RBD-targeting IGHV3-

217   53 antibodies with longer CDR H3s should further aid in explaining the differential

218   occurrence frequency between binding modes A and B.

219

9

220   Given the large number of neutralizing antibodies currently being identified (Andreano et

221   al., 2020; Brouwer et al., 2020; Cao et al., 2020; Chi et al., 2020; Ju et al., 2020; Kreer et

222   al., 2020; Robbiani et al., 2020; Rogers et al., 2020; Seydoux et al., 2020; Zost et al.,

223   2020), structural understanding of the antigenicity and immunogenicity of SARS-CoV-2 S

224   protein is still at an early stage. It is clear that antibodies are elicited to the RBD in natural

225   infection. As SARS-CoV-2 may eventually become endemic within the human population

226   (Li et al., 2020) and escape mutations may arise, the structural information elucidated here

227   can be harnessed for modifying or improving existing vaccine designs, and for assessing

228   the quality and efficacy of vaccine responses.

229

245

246 **AUTHOR CONTRIBUTIONS**

247 N.C.W., M.Y., H.L. and I.A.W. conceived and designed the study. N.C.W., M.Y., H.L. and

248 C.C.D.L. expressed and purified the proteins. T.G.C., P.J.M.B., M.J.v.G. and R.W.S.

249 provided antibody clones and sequences. S.B., J.L.T., and A.B.W provided the nsEM

250 maps and performed fitting. N.C.W., M.Y., H.L. and X.Z. performed the crystallization, X-

251 ray data collection, determined and refined the X-ray structures. N.C.W., M.Y., H.L.,

252 C.C.D.L., X.Z. and I.A.W. analyzed the data. N.C.W., M.Y., H.L. and I.A.W. wrote the

253 paper and all authors reviewed and/or edited the paper.

254

255 **COMPETING INTERESTS**

256 Amsterdam UMC previously filed a patent application that included SARS-CoV-2

257 antibodies COVA2-04 and COVA2-39 (Brouwer et al., 2020).

258

259

Fig. 1

260
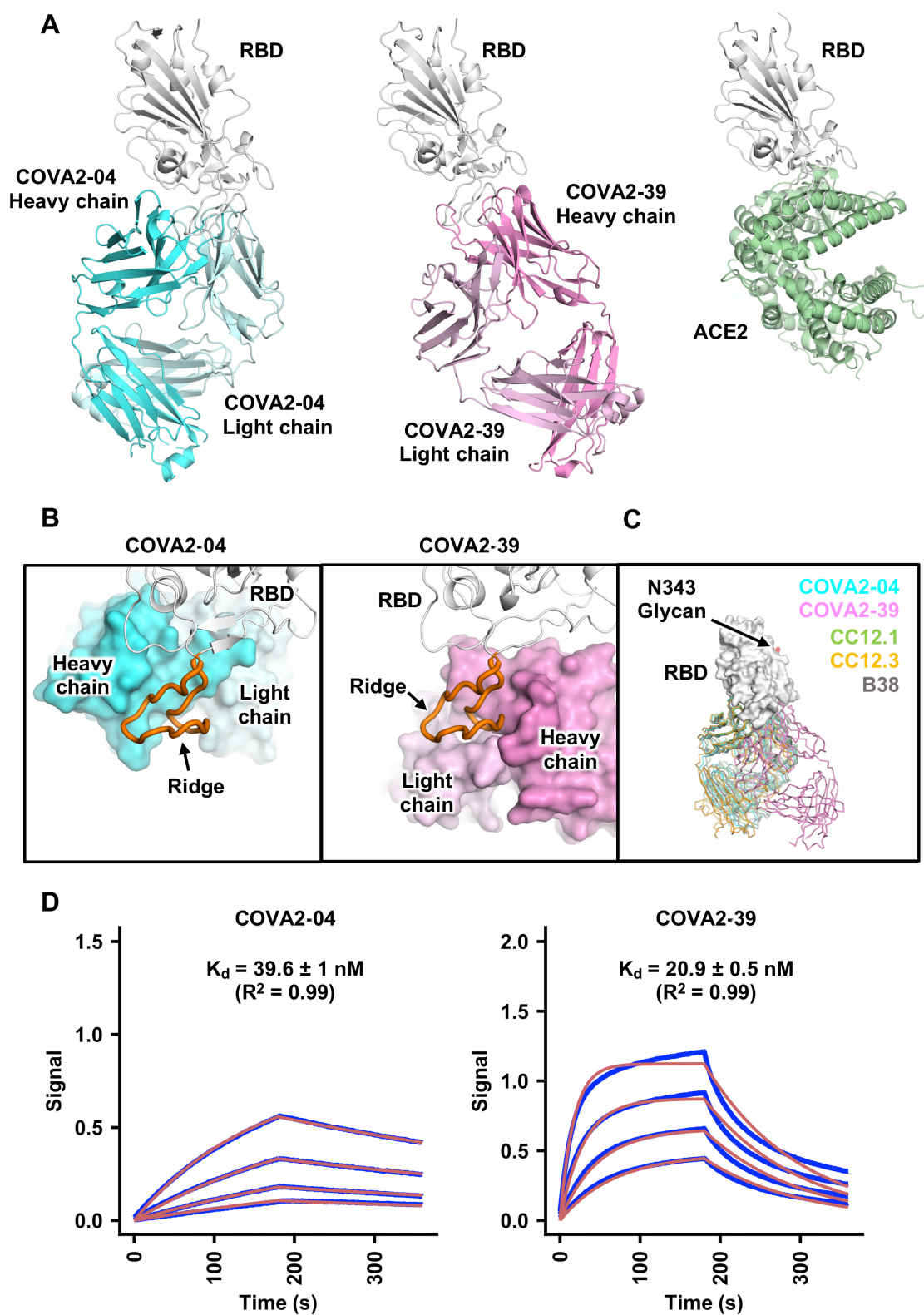
261 **Figure 1. Structures of two IGHV3-53 antibodies to SARS-CoV-2 RBD with very**

262 **different binding modes. (A)** Crystal structures of COVA2-04/RBD and COVA2-39/RBD

263 complexes are shown. Human ACE2/RBD complex is also shown for comparison (PDB

264 6M0J) (Lan et al., 2020). **(B)** Zoomed-in views of COVA2-04/RBD (left) and COVA2-

265 39/RBD (right) interfaces are shown. COVA2-04 (cyan) and COVA2-39 (pink) are shown

266 in surface representation, and RBD (white) in a cartoon representation in the same view

267 as **A**. The ACE2-binding ridge in the RBD is in orange. **(C)** Binding modes of COVA2-04

268 (cyan), COVA2-39 (pink), CC12.1 (green), CC12.3 (orange), and B38 (gray) to SARS-

269 CoV-2 (white) are compared in the same view as in **A** and **B**. CC12.1/RBD and

270 CC12.3/RBD complexes are from PDB 6XC3 and PDB 6XC4, respectively (Yuan et al.,

271 2020a), and RBD B38/RBD complex from PDB 7BZ5 (Wu et al., 2020). The N-glycan

272 observed at SARS-CoV-2 RBD N343, which is distant from the epitopes of COVA2-04

273 and COVA2-39, is shown in red. **(E)** Binding kinetics of COVA2-04 and COVA2-39 Fabs

274 against SARS-CoV-2 RBD were measured by biolayer interferometry (BLI). Y-axis

275 represents the response. Blue lines represent the response curves and red lines represent

276 a 1:1 binding model. Binding kinetics were measured for four concentrations of each Fab

277 at 2-fold dilution starting from 125 nM. The K_d and R^2 of the fitting are indicated.

278 Representative results of two replicates are shown here.

279

Fig. 2

A   COVA2-04

B   COVA2-39

C   ACE2

280

14
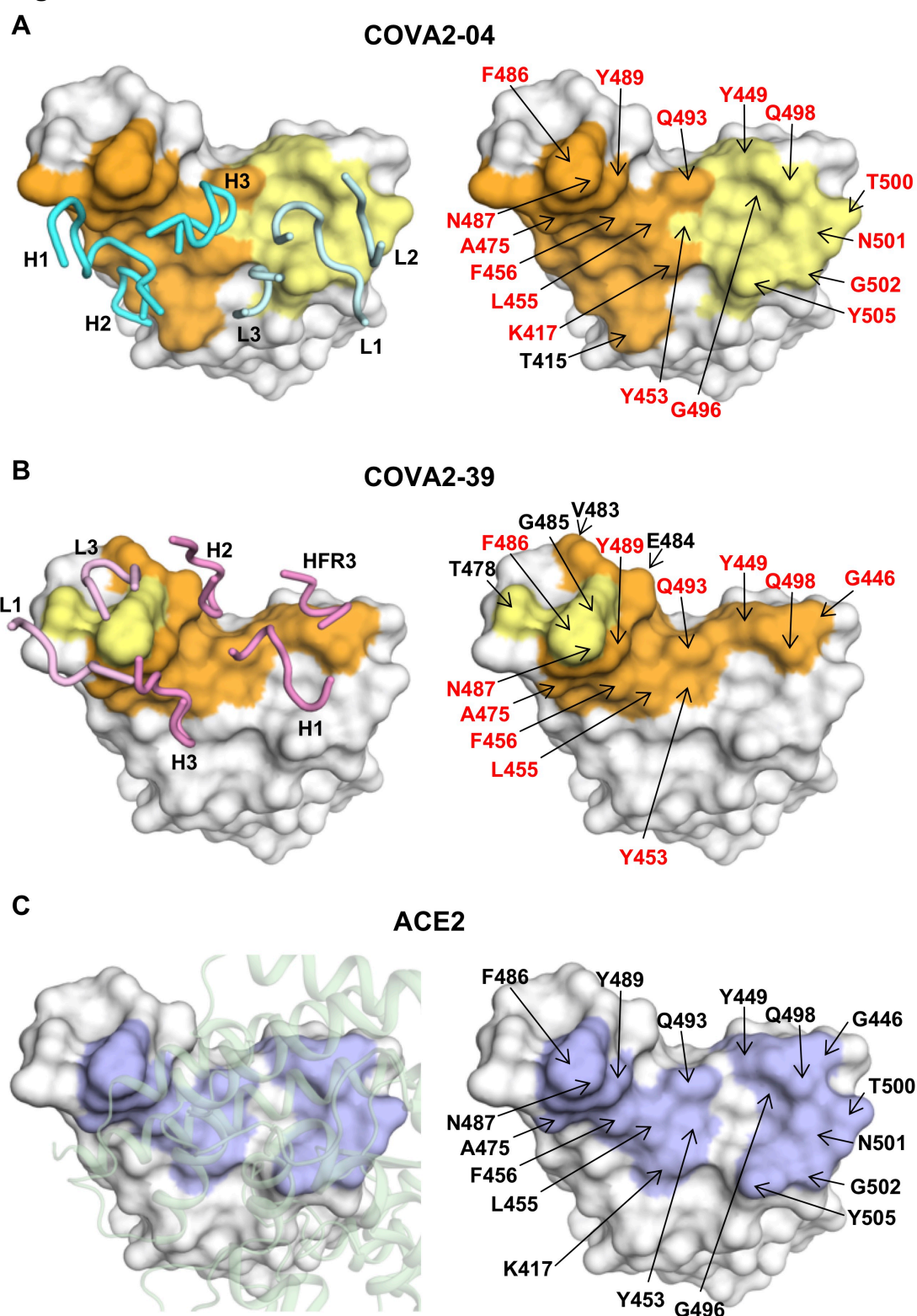
281 **Figure 2. Epitopes of COVA2-04 and COVA2-39. (A-B)** Epitope residues of **(A)** COVA2-

282 04, and **(B)** COVA2-39 are identified by PISA (Krissinel and Henrick, 2007). Epitope

283 residues contacting the heavy chain are in orange and light chain in yellow. On the left

284 panels, CDR loops are labeled. On the right panels, epitope residues are labeled. For

285 clarity, only representative epitope residues are labeled. Epitope residues that are also

286 involved in ACE2 binding are in red. **(C)** ACE2-binding residues on the RBD are shown in

287 blue. On the left panel, ACE2 is shown in green within a semi-transparent surface

288 representation. On the right panel, ACE2-binding residues are labeled. A total of 17

289 residues in the SARS-CoV-2 RBD are used for binding by ACE2 (Lan et al., 2020). The

290 17 ACE2-binding residues are as described previously (Lan et al., 2020).

15

Fig. 3

291
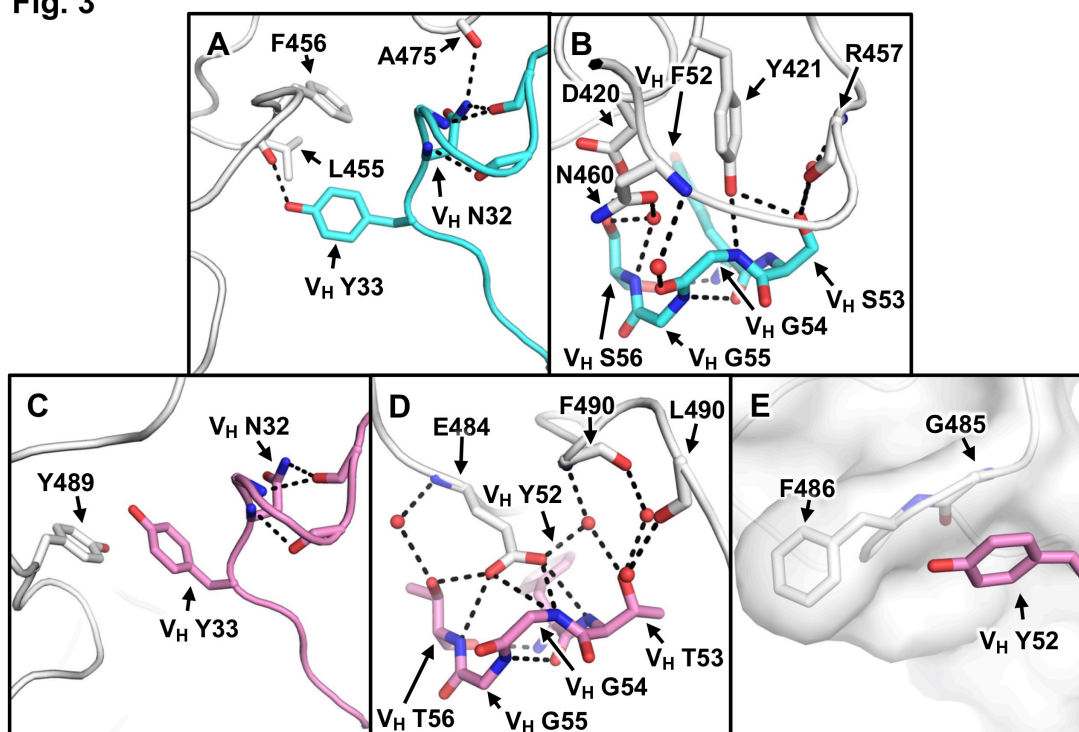
Figure 3. Heavy chain interactions of COVA2-39 and COVA2-04 with the RBD. (A, C) Interactions are shown between RBD (white) and signature $_{32}NY_{33}$ motifs on the CDR H1 loop of VH3-53 antibodies **(A)** COVA2-04 (cyan), and **(C)** COVA2-39. **(B, D)** RBD forms an extensive hydrogen bonding network with **(B)** $_{53}SGGS_{56}$ motif on the CDR H2 loop of COVA2-04, and **(D)** $_{53}TGGT_{56}$ motif on the CDR H2 loop of COVA2-39. **(F)** A π−π interaction is illustrated between G485 peptide backbone in the RBD (semi-transparent white surface) and V_H Y52. Hydrogen bonds are represented by dashed lines and water molecules by red spheres.

Fig. 4

D

Structures available

CDR H3

COVA2-04: DLERAGGM-DV
CC12.1: DLDVYGL--DV
CC12.3: DFGDFYF--DY
B38: EAYGM----DV
C105: GEGWELPY-DY
COVA2-07: AREAYGM--DV
BD-494: ARDLVVYGMDV

300
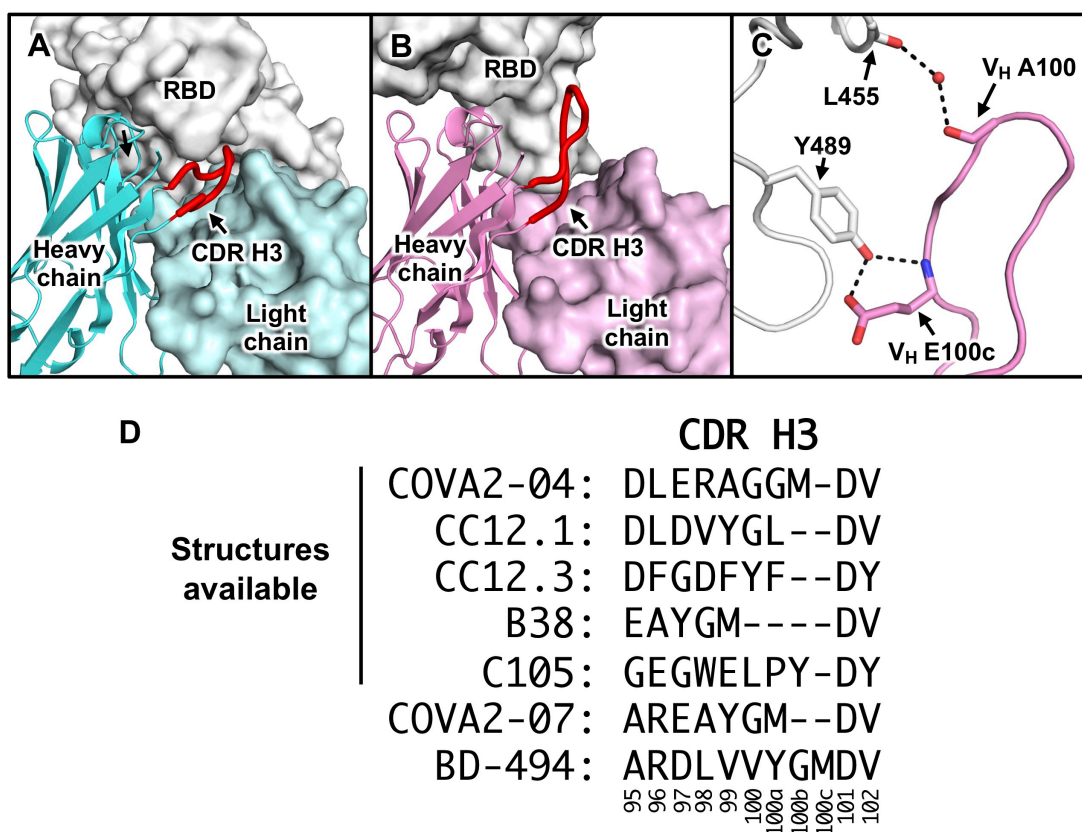
301 **Figure 4. Structural constraints of CDR H3 length in different binding modes of**

302 **IGHV3-53 antibodies. (A)** Interaction between COVA2-04 (cyan) and the RBD (white) is

303 shown with CDR H3 highlighted in red. **(B)** Interaction between COVA2-39 (pink) and the

304 RBD (white) is shown with CDR H3 highlighted in red. In this view, the RBD is rotated

305 ~180° relative to (**A**). **(C)** CDR H3 of COVA2-39 makes very few contacts with the RBD.

306 Hydrogen bond interactions are represented by dashed lines and water molecules by red

307 spheres. **(D)** CDR H3 sequences are compared for COVA2-04, CC12.1 (Yuan et al.,

308 2020a), CC12.3 (Yuan et al., 2020a), B38 (Wu et al., 2020), C105 (Barnes et al., 2020),

309 COVA2-07 (Brouwer et al., 2020), and BD-494 (Cao et al., 2020). Of note, BD-494 belongs

310 to a cluster of RBD-targeting IGHV3-53 antibodies with similar CDR H3 sequences,

311 including BD500, BD-503, BD-505, BD-506, BD-507, and BD-508 (Cao et al., 2020).

312 Residue positions are labeled according to the Kabat numbering scheme.

17

Fig. 5
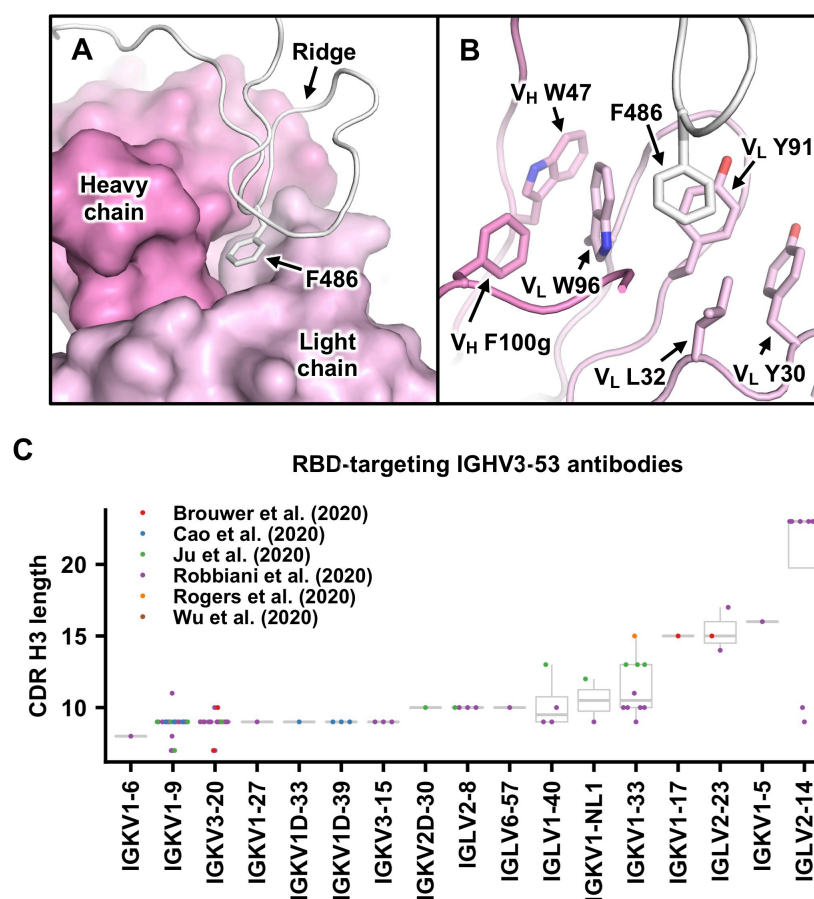
Figure 5. Structural analysis of the RBD ridge-anchoring pocket in COVA2-39. (A) The ACE2-binding ridge of the RBD (white) is shown in a cartoon representation. F486 at the tip of the ridge is shown as a stick representation and COVA2-39 Fab in a surface representation. **(B)** Interaction between F486 and COVA2-39 in the ridge-anchoring pocket is shown. **(C)** CDR H3 length of previously discovered RBD-targeting IGHV3-53 antibodies is summarized (Brouwer et al., 2020; Cao et al., 2020; Ju et al., 2020; Rogers et al., 2020; Wu et al., 2020). The light chain genes for these antibodies are shown in the bottom panel.

322   **MATERIALS AND METHODS**

323   **Expression and purification of SARS-CoV-2 RBD**

324   The receptor-binding domain (RBD) (residues 319-541) of the SARS-CoV-2 spike (S)

325   protein (GenBank: QHD43416.1) was cloned into a customized pFastBac vector (Ekiert

326   et al., 2011), and fused with an N-terminal gp67 signal peptide and C-terminal His$_6$ tag

327   (Yuan et al., 2020b). A recombinant bacmid DNA was generated using the Bac-to-Bac

328   system (Life Technologies). Baculovirus was generated by transfecting purified bacmid

329   DNA into Sf9 cells using FuGENE HD (Promega), and subsequently used to infect

330   suspension cultures of High Five cells (Life Technologies) at an MOI of 5 to 10. Infected

331   High Five cells were incubated at 28 °C with shaking at 110 r.p.m. for 72 h for protein

332   expression. The supernatant was then concentrated using a 10 kDa MW cutoff

333   Centramate cassette (Pall Corporation). The RBD protein was purified by Ni-NTA,

334   followed by size exclusion chromatography, and buffer exchanged into 20 mM Tris-HCl

335   pH 7.4 and 150 mM NaCl.

336

337   **Expression and purification of Fabs**

338   For COVA2-04 and COVA2-39, the heavy and light chains were cloned into phCMV3. The

339   plasmids were transiently co-transfected into ExpiCHO cells at a ratio of 2:1 (HC:LC) using

340   ExpiFectamine™ CHO Reagent (Thermo Fisher Scientific) according to the

341   manufacturer's instructions. The supernatant was collected at 10 days post-transfection.

342   The Fabs were purified with a CaptureSelect™ CH1-XL Affinity Matrix (Thermo Fisher

343   Scientific) followed by size exclusion chromatography.

344

345   **Crystallization and structural determination**

346   COVA2-04/RBD and COVA2-39/RBD complexes were formed by mixing each of the

347   protein components at an equimolar ratio and incubated overnight at 4°C. Each complex

19

348   was adjusted to 12 mg/ml and screened for crystallization using the 384 conditions of the

349   JCSG Core Suite (Qiagen) on our custom-designed robotic CrystalMation system

350   (Rigaku) at Scripps Research. Crystallization trials were set-up by the vapor diffusion

351   method in sitting drops containing 0.1 µl of protein and 0.1 µl of reservoir solution.

352   Diffraction-quality crystals were obtained in the following conditions:

353

354   COVA2-04/RBD complex (12 mg/mL): 8.5% isopropanol, 10% ethylene glycol, 15%

355   glycerol, 0.085 M HEPES pH 7.5, and 17% polyethylene glycol 4000 at 20 °C.

356   COVA2-39/RBD complex (12 mg/mL): 0.1 M sodium citrate pH 5.6, 20% isopropanol, 10%

357   ethylene glycol, and 20% polyethylene glycol 4000 at 20 °C.

358

359   All crystals appeared on day 3, harvested on day 7, and were then flash cooled and stored

360   in liquid nitrogen until data collection. Diffraction data were collected at cryogenic

361   temperature (100 K) at Stanford Synchrotron Radiation Lightsource (SSRL) on the new

362   Scripps/Stanford beamline 12-1 with a beam wavelength of 0.97946 Å, and processed

363   with HKL2000 (Otwinowski and Minor, 1997). Structures were solved by molecular

364   replacement using PHASER (McCoy et al., 2007). The models for molecular replacement

365   of RBD and COVA2-04 were from PBD 6XC4 (Yuan et al., 2020a), whereas the model of

366   COVA2-39 was generated by Repertoire Builder (https://sysimm.ifrec.osaka-

367   u.ac.jp/rep_builder/) (Schritt et al., 2019). Iterative model building and refinement were

368   carried out in COOT (Emsley et al., 2010) and PHENIX (Adams et al., 2010), respectively.

369   Epitope and paratope residues, as well as their interactions, were identified by accessing

370   PISA (Proteins, Interfaces, Structures and Assemblies) at the European Bioinformatics

371   Institute (http://www.ebi.ac.uk/pdbe/prot_int/pistart.html) (Krissinel and Henrick, 2007).

372

373   **Biolayer interferometry binding assay**

20

374   Antibody binding and competition assays were performed by biolayer interferometry (BLI)

375   using an Octet Red instrument (FortéBio) as described previously (Wu et al., 2017), with

376   anti-human Fab-CH1 2nd generation (FAB2G) biosensors. There were five steps in the

377   assay: 1) baseline: 60 s with 1x kinetics buffer; 2) loading: 240 s with 50 µg/mL of COVA2-

378   04 Fab or COVA2-39 Fab; 3) baseline: 60 s with 1x kinetics buffer; 4) association: 180 s

379   with serial diluted concentrations of SARS-CoV-2 RBD; and 5) dissociation: 180 s with 1x

380   kinetics buffer. For K_d estimation, a 1:1 binding model was used.

381

382   **Data availability**

383   X-ray coordinates and structure factors are being deposited in the RCSB Protein Data

384   Bank.

385

386   **REFERENCES**

387   Adams, P.D., Afonine, P.V., Bunkoczi, G., Chen, V.B., Davis, I.W., Echols, N., Headd,
388   J.J., Hung, L.W., Kapral, G.J., Grosse-Kunstleve, R.W., *et al.* (2010). PHENIX: a
389   comprehensive Python-based system for macromolecular structure solution. Acta
390   Crystallogr D Biol Crystallogr *66*, 213-221.

391   Andreano, E., Nicastri, E., Paciello, I., Pileri, P., Manganaro, N., Piccini, G., Manenti, A.,
392   Pantano, E., Kabanova, A., Troisi, M., *et al.* (2020). Identification of neutralizing human
393   monoclonal antibodies from Italian Covid-19 convalescent patients. bioRxiv
394   10.1101/2020.05.05.078154.

395   Barnes, C.O., West, A.P., Huey-Tubman, K.E., Hoffmann, M.A.G., Sharaf, N.G.,
396   Hoffman, P.R., Koranda, N., Gristick, H.B., Gaebler, C., Muecksch, F., *et al.* (2020).
397   Structures of human antibodies bound to SARS-CoV-2 spike reveal common epitopes
398   and recurrent features of antibodies. Cell 10.1016/j.cell.2020.06.025.

399   Brouwer, P.J.M., Caniels, T.G., van der Straten, K., Snitselaar, J.L., Aldon, Y., Bangaru,
400   S., Torres, J.L., Okba, N.M.A., Claireaux, M., Kerster, G., *et al.* (2020). Potent
401   neutralizing antibodies from COVID-19 patients define multiple targets of vulnerability.
402   Science 10.1126/science.abc5902.

403   Cao, Y., Su, B., Guo, X., Sun, W., Deng, Y., Bao, L., Zhu, Q., Zhang, X., Zheng, Y.,
404   Geng, C., *et al.* (2020). Potent neutralizing antibodies against SARS-CoV-2 identified by
405   high-throughput single-cell sequencing of convalescent patients' B cells. Cell *182*, 73-84.

406　Chi, X., Yan, R., Zhang, J., Zhang, G., Zhang, Y., Hao, M., Zhang, Z., Fan, P., Dong, Y.,
407　Yang, Y., *et al.* (2020). A neutralizing human antibody binds to the N-terminal domain of
408　the Spike protein of SARS-CoV-2. Science *368*, 1274-1278.

409　Ekiert, D.C., Friesen, R.H., Bhabha, G., Kwaks, T., Jongeneelen, M., Yu, W., Ophorst,
410　C., Cox, F., Korse, H.J., Brandenburg, B., *et al.* (2011). A highly conserved neutralizing
411　epitope on group 2 influenza A viruses. Science *333*, 843-850.

412　Ekiert, D.C., Kashyap, A.K., Steel, J., Rubrum, A., Bhabha, G., Khayat, R., Lee, J.H.,
413　Dillon, M.A., O'Neil, R.E., Faynboym, A.M., *et al.* (2012). Cross-neutralization of
414　influenza A viruses mediated by a single antibody loop. Nature *489*, 526-532.

415　Emsley, P., Lohkamp, B., Scott, W.G., and Cowtan, K. (2010). Features and
416　development of Coot. Acta Crystallogr D Biol Crystallogr *66*, 486-501.

417　Ju, B., Zhang, Q., Ge, J., Wang, R., Sun, J., Ge, X., Yu, J., Shan, S., Zhou, B., Song, S.,
418　*et al.* (2020). Human neutralizing antibodies elicited by SARS-CoV-2 infection. Nature
419　10.1038/s41586-020-2380-z.

420　Kreer, C., Zehner, M., Weber, T., Rohde, C., Halwe, S., Ercanoglu, M.S., Gieselmann,
421　L., Korenkov, M., Gruell, H., Schommers, P., *et al.* (2020). Longitudinal isolation of
422　potent near-germline SARS-CoV-2-neutralizing antibodies from COVID-19 patients. Cell
423　10.1016/j.cell.2020.06.044.

424　Krissinel, E., and Henrick, K. (2007). Inference of macromolecular assemblies from
425　crystalline state. J Mol Biol *372*, 774-797.

426　Lan, J., Ge, J., Yu, J., Shan, S., Zhou, H., Fan, S., Zhang, Q., Shi, X., Wang, Q., Zhang,
427　L., *et al.* (2020). Structure of the SARS-CoV-2 spike receptor-binding domain bound to
428　the ACE2 receptor. Nature *581*, 215-220.

429　Lee, P.S., Ohshima, N., Stanfield, R.L., Yu, W., Iba, Y., Okuno, Y., Kurosawa, Y., and
430　Wilson, I.A. (2014). Receptor mimicry by antibody F045-092 facilitates universal binding
431　to the H3 subtype of influenza virus. Nat Commun *5*, 3614.

432　Li, R., Pei, S., Chen, B., Song, Y., Zhang, T., Yang, W., and Shaman, J. (2020).
433　Substantial undocumented infection facilitates the rapid dissemination of novel
434　coronavirus (SARS-CoV-2). Science *368*, 489-493.

435　McCoy, A.J., Grosse-Kunstleve, R.W., Adams, P.D., Winn, M.D., Storoni, L.C., and
436　Read, R.J. (2007). Phaser crystallographic software. J Appl Crystallogr *40*, 658-674.

437　Otwinowski, Z., and Minor, W. (1997). Processing of X-ray diffraction data collected in
438　oscillation mode. Methods Enzymol *276*, 307-326.

439　Robbiani, D.F., Gaebler, C., Muecksch, F., Lorenzi, J.C.C., Wang, Z., Cho, A., Agudelo,
440　M., Barnes, C.O., Gazumyan, A., Finkin, S., *et al.* (2020). Convergent antibody
441　responses to SARS-CoV-2 in convalescent individuals. Nature 10.1038/s41586-020-
442　2456-9.

443   Rogers, T.F., Zhao, F., Huang, D., Beutler, N., Burns, A., He, W.-t., Limbo, O., Smith, C.,
444   Song, G., Woehl, J., *et al.* (2020). Isolation of potent SARS-CoV-2 neutralizing
445   antibodies and protection from disease in a small animal model. Science
446   10.1126/science.abc7520.

447   Schritt, D., Li, S., Rozewicki, J., Katoh, K., Yamashita, K., Volkmuth, W., Cavet, G., and
448   Standley, D.M. (2019). Repertoire Builder: high-throughput structural modeling of B and
449   T cell receptors. Mol Syst Des Eng *4*, 761-768.

450   Seydoux, E., Homad, L.J., MacCamy, A.J., Parks, K.R., Hurlburt, N.K., Jennewein, M.F.,
451   Akins, N.R., Stuart, A.B., Wan, Y.-H., Feng, J., *et al.* (2020). Analysis of a SARS-CoV-2-
452   infected individual reveals development of potent neutralizing antibodies with limited
453   somatic mutation. Immunity *53*, 98-105.

454   Shi, R., Shan, C., Duan, X., Chen, Z., Liu, P., Song, J., Song, T., Bi, X., Han, C., Wu, L.,
455   *et al.* (2020). A human neutralizing antibody targets the receptor binding site of SARS-
456   CoV-2. Nature 10.1038/s41586-020-2381-y.

457   Walls, A.C., Park, Y.J., Tortorici, M.A., Wall, A., McGuire, A.T., and Veesler, D. (2020).
458   Structure, function, and antigenicity of the SARS-CoV-2 spike glycoprotein. Cell *181*,
459   281-292.e286.

460   Wrapp, D., Wang, N., Corbett, K.S., Goldsmith, J.A., Hsieh, C.L., Abiona, O., Graham,
461   B.S., and McLellan, J.S. (2020). Cryo-EM structure of the 2019-nCoV spike in the
462   prefusion conformation. Science *367*, 1260-1263.

463   Wu, N.C., Grande, G., Turner, H.L., Ward, A.B., Xie, J., Lerner, R.A., and Wilson, I.A.
464   (2017). In vitro evolution of an influenza broadly neutralizing antibody is modulated by
465   hemagglutinin receptor specificity. Nat Commun *8*, 15371.

466   Wu, Y., Wang, F., Shen, C., Peng, W., Li, D., Zhao, C., Li, Z., Li, S., Bi, Y., Yang, Y., *et*
467   *al.* (2020). A noncompeting pair of human neutralizing antibodies block COVID-19 virus
468   binding to its receptor ACE2. Science *368*, 1274-1278.

469   Yuan, M., Liu, H., Wu, N.C., Lee, C.-C.D., Zhu, X., Zhao, F., Huang, D., Yu, W., Hua, Y.,
470   Tien, H., *et al.* (2020a). Structural basis of a shared antibody response to SARS-CoV-2.
471   Science 10.1101/2020.06.08.141267.

472   Yuan, M., Wu, N.C., Zhu, X., Lee, C.D., So, R.T.Y., Lv, H., Mok, C.K.P., and Wilson, I.A.
473   (2020b). A highly conserved cryptic epitope in the receptor-binding domains of SARS-
474   CoV-2 and SARS-CoV. Science *368*, 630-633.

475   Zost, S.J., Gilchuk, P., Chen, R.E., Case, J.B., Reidy, J.X., Trivette, A., Nargi, R.S.,
476   Sutton, R.E., Suryadevara, N., Chen, E.C., *et al.* (2020). Rapid isolation and profiling of
477   a diverse panel of human monoclonal antibodies targeting the SARS-CoV-2 spike
478   protein. Nat Med 10.1101/2020.05.12.091462.
479

A

```
                                                      CDR H1
COVA2-39:  QVQLVETGGGLIQPGGSLRLSCAASGFTVSSNYMSWVRQAP
COVA2-04:  QVQLVETGGGLIQPGGSLRLSCAASGFTVSSNYMSWVRQAP
IGHV3-53:  EVQLVETGGGLIQPGGSLRLSCAASGFTVSSNYMSWVRQAP
                                            31 32 33 34 35
```

```
                         CDR H2
COVA2-39:  GKGLEWVSVIYTGGTTYYADSVKGRFTISRDNSKNTLYLQM
COVA2-04:  GKGLEWVSVIYSGGSTFYADSVKGRFTISRDNSKNTLYLQM
IGHV3-53:  GKGLEWVSVIYSGGSTYYADSVKGRFTISRDNSKNTLYLQM
                     50 51 52 53 54 55 56 57 58 59 60 61 62 63 64 65
```

```
                              CDR3 H3
COVA2-39:  NSLRAEDTAVYYCARAHVDTAMVESGAFDIWGQGTRVTVSS
COVA2-04:  NSLRAEDTAVYYCARDLERAGGM-----DVWGQGTMVTVSS
IGHV3-53:  NSLRAEDTAVYYCAR--------------------------
                   95 96 97 98 99 100 100a 100b 100c 100d 100e 100f 100g 101 102
```

B

```
                                                  CDR L1
COVA2-04:  EIVMTQSPGTLSLSPGERATLSCRASQSVSSSYLAWYQQK
IGKV3-20:  EIVLTQSPGTLSLSPGERATLSCRASQSVSSSYLAWYQQK
                                        24 25 26 27 27a 28 29 30 31 32 33 34
```

```
                         CDR L2
COVA2-04:  PGQAPRLLIYGASSRATGIPDRFSGSGSGTDFTLTISRLE
IGKV3-20:  PGQAPRLLIYGASSRATGIPDRFSGSGSGTDFTLTISRLE
                         50 51 52 53 54 55 56
```

```
                         CDR L3
COVA2-04:  PEDFAVYYCQQYGSLYTFGQGTKVDIK
IGKV3-20:  PEDFAVYYCQQYGS-------------
                      89 90 91 92 93 94 96 97
```

C

```
                                                  CDR L1
COVA2-39:  QSALTQPASVSGSPGQSITISCTGTSSDVGSYNLVSWYQQ
IGLV2-23:  QSALTQPASVSGSPGQSITISCTGTSSDVGSYNLVSWYQQ
                                    24 25 26 27 27a 27b 27c 28 29 30 31 32 33 34
```

```
                         CDR L2
COVA2-39:  HPGKAPKLMIYEVTKRPSGVSNRFSGSKSGNTASLTISGL
IGLV2-23:  HPGKAPKLMIYEVSKRPSGVSNRFSGSKSGNTASLTISGL
                         50 51 52 53 54 55 56
```

```
                         CDR L3
COVA2-39:  QAEDEADYYCCSYAGSSTWVFGGGTKLTVL
IGLV2-23:  QAEDEADYYCCSYAGSSTF-----------
                      89 90 91 92 93 94 95 95a 96 97
```

1

2   **Supplementary Figure 1. Comparison of COVA2-04 and COVA2-39 sequences to**

3   **germline sequences. (A)** Alignment of the heavy-chain variable domain sequences of

1

4   COVA2-04 and COVA2-39 with the germline IGHV3-53 sequence **(B)** Alignment of the

5   light-chain variable domain sequence of COVA2-04 with the germline IGKV3-20

6   sequence. **(C)** Alignment of the light-chain variable domain sequence of COVA2-39 with

7   the germline IGLV2-23 sequence. The regions that correspond to CDR H1, H2, H3, L1,

8   L2, and L3 are indicated. Residues that differ from the germline are highlighted in red.

9   Residue positions in the CDRs are labeled according to the Kabat numbering scheme.

10   Residues that interact with the RBD are highlighted in yellow.

11

12
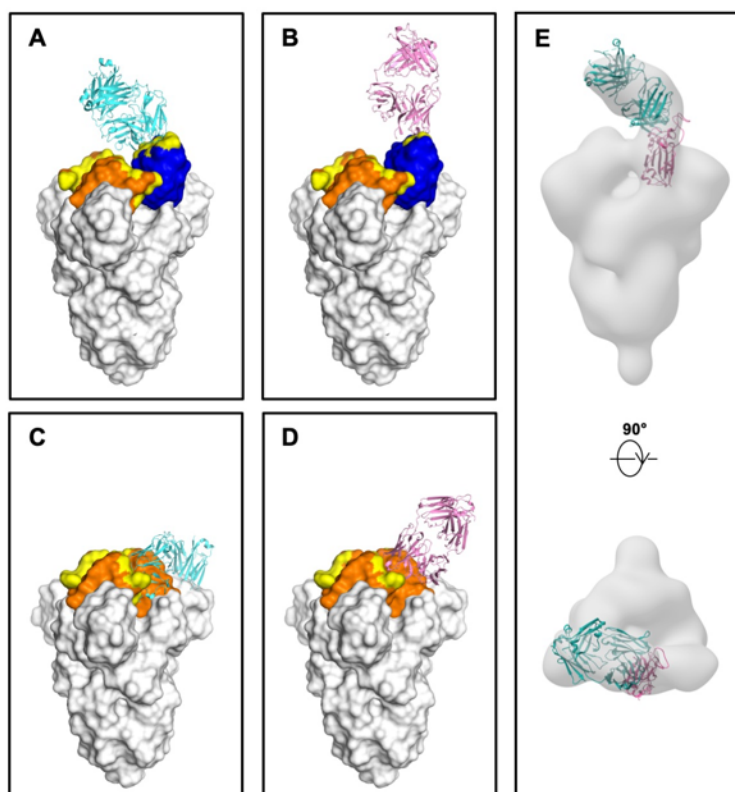
Supplementary Figure 2. Modelling the binding of COVA2-39 and COVA2-04 on the homotrimeric SARS CoV-2 spike (S) protein. (A-B) The SARS-CoV-2 S trimer is shown with one RBD in the up conformation (cyan) and two RBDs in the down conformation (orange) (PDB: 6VSB) (Wrapp et al., 2020). Binding of **(A)** COVA2-04 (cyan) and **(B)** COVA2-39 (pink) to the RBDs in the up conformations is modelled. **(C-D)** The SARS-CoV-2 S trimer is shown with all three RBD in down conformations (PDB 6VXX) (Walls et al., 2020). **(C)** COVA2-04 (cyan) and **(D)** COVA2-39 (pink) cannot bind to their epitopes in the RBD in the down conformation as the epitopes are partially buried. Epitopes are colored in yellow. **(E)** COVA2-04/RBD crystal structure was fitted here to the negative-stain electron microscopy (nsEM) reconstruction of the Fab COVA-2-04/SARS CoV-2 spike protein complex that was previously generated (Brouwer et al., 2020). A similar analysis was not performed with the COVA2-39/RBD because of the poorer quality of nsEM map

3

25   of the COVA2-39/S protein complex (Brouwer et al., 2020).

26
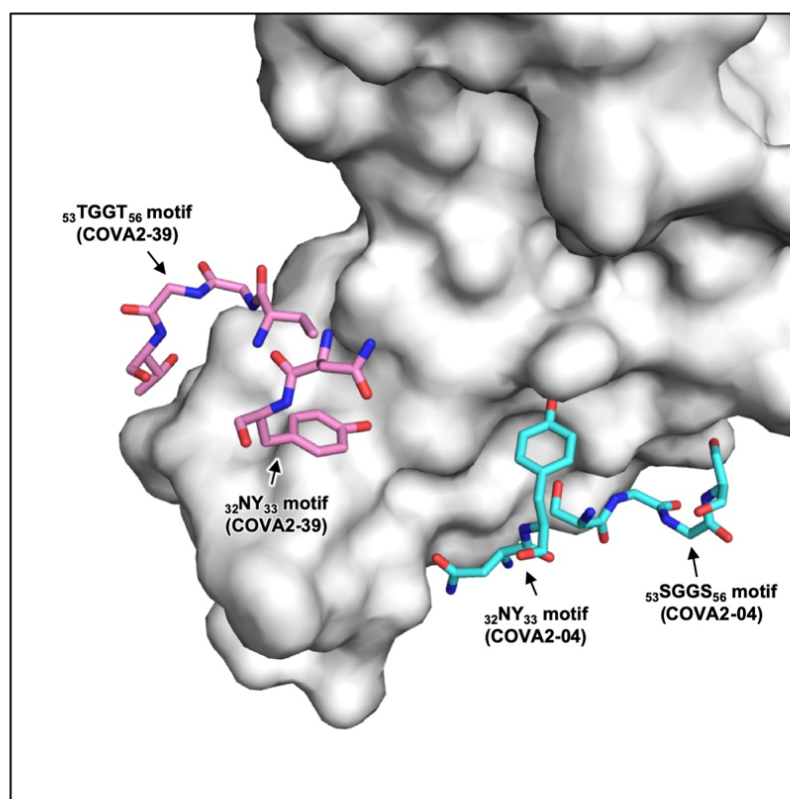
Supplementary Figure 3. Locations of $_{32}NY_{33}$ motif and $_{53}SGGS_{56}$ ($_{53}TGGT_{56}$) motifs when VH3-53 antibodies bind the SARS CoV-2 RBD. The locations of $_{32}NY_{33}$ motif and $_{53}SGGS_{56}$ motif in COVA2-04 (cyan) as well as $_{32}NY_{33}$ motif and $_{53}TGGT_{56}$ motif in COVA2-39 (pink) are shown. SARS-CoV-2 RBD is shown as a white surface.

31
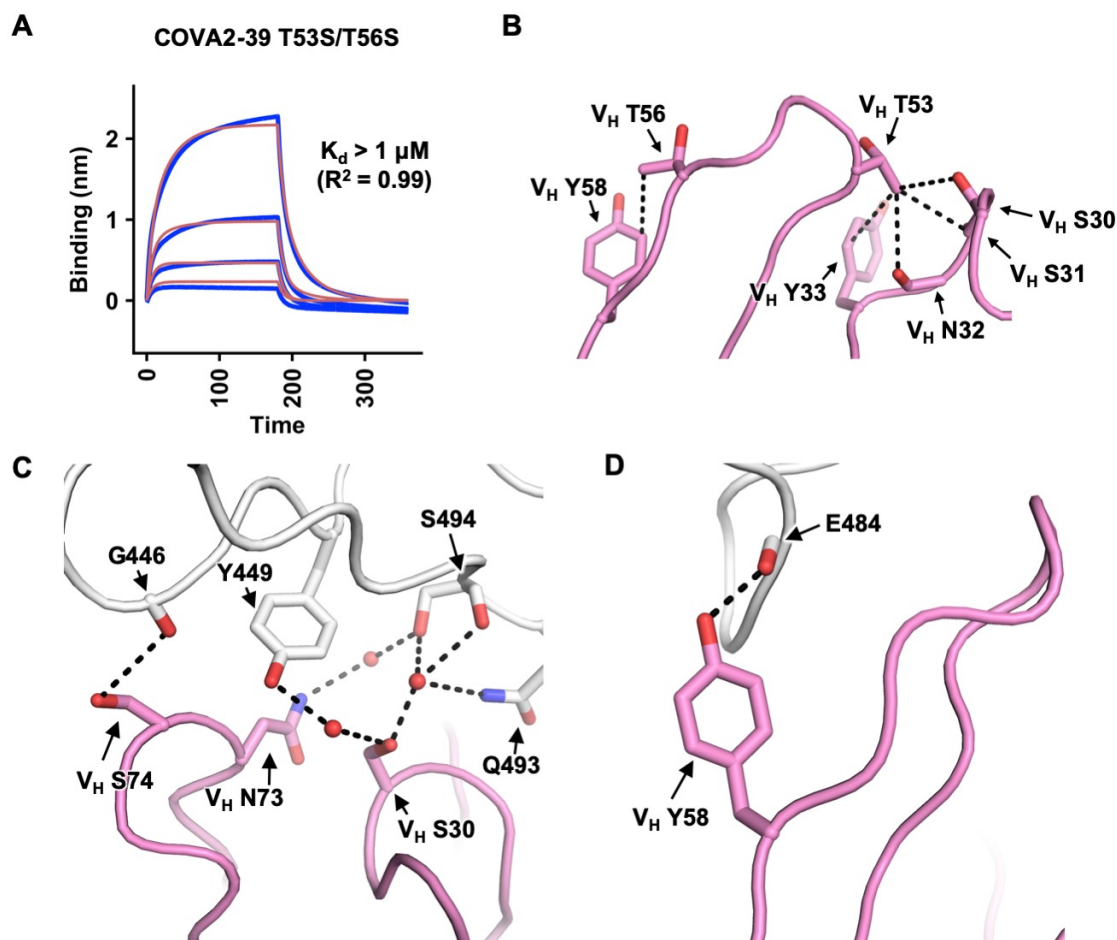
Supplementary Figure 4. Key interactions between COVA2-39 and RBD. (A) Binding

kinetics of COVA2-39 T53S/T56S somatic revertant in Fab format to SARS-CoV-2 RBD

were measured by biolayer interferometry (BLI). Y-axis represents the response and blue

lines represent the response curves. A 1:1 binding model did not fit very well, potentially

due to some contribution of non-specific binding to the response curve. Subsequently, a

2:1 heterogeneous ligand model was used to improve the fit, which is represented by the

red lines. In both models, the K_d estimated is > 1 µM. Binding kinetics were measured for

four concentrations of each Fab at 2-fold dilution starting from 500 nM. The K_d and R^2 of

the fitting are indicated. Representative result of two replicates is shown here. **(B)** Van der

Waals Interactions (within a distance of 4 Å, dashed lines) that involve the methyl group

of V_H T53 and V_H T56 of COVA2-39 are shown. **(C)** The hydroxyl side chain of V_H S30

6

43   interacts with RBD Y449, Q493, and S494 through water-mediated H-bonds. The side

44   chain of V_H N73 interacts with RBD S494 through a water-mediated H-bond. The side

45   chain of V_H S74 H-bonds with the backbone carbonyl of RBD G446. **(D)** The side chain of

46   V_H Y58 H-bonds with the backbone carbonyl of RBD E484. Hydrogen bonds are

47   represented by dashed lines and water molecules by red spheres.

48
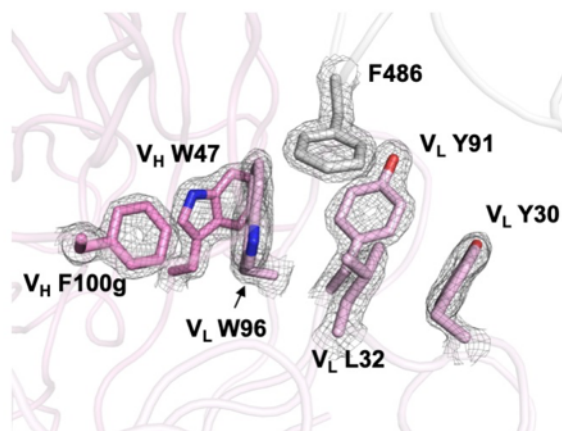
Supplementary Figure 5. Electron density maps for the ridge-anchoring pocket.
Final 2Fo-Fc electron density map for the ridge-anchoring pocket around RBD F486 is contoured at 2.0 σ.

52   **Supplementary Table 1. X-ray data collection and refinement statistics**

Data collection		
	COVA2-04 + RBD	COVA2-39 + RBD
Beamline	SSRL 12-1	SSRL 12-1
Wavelength (Å)	0.97946	0.97946
Space group	C 1 2 1	P 1 2_1 1
Unit cell parameters		
a, b, c (Å)	197.2, 84.7, 57.3	68.9, 80.4, 72.0
α, β, γ (°)	90, 99.6, 90	90, 104.9, 90
Resolution (Å) [a]	50.0–2.35 (2.39–2.35)	50.0–1.72 (1.75–1.72)
Unique reflections [a]	37,264 (3,371)	79,114 (7,573)
Redundancy [a]	2.9 (2.0)	1.9 (1.8)
Completeness (%) [a]	97.2 (88.6)	97.2 (97.6)
$<I/\sigma_I>$ [a]	5.4 (1.1)	26.2 (1.1)
R_{sym} [b] (%) [a]	16.3 (89.8)	5.7 (93.4)
R_{pim} [b] (%) [a]	7.2 (47.0)	3.2 (57.6)
$CC_{1/2}$ [c] (%) [a]	98.5 (67.7)	99.6 (50.6)
Refinement statistics		
Resolution (Å)	48.6–2.35	34.8–1.72
Reflections (work)	37,264	79,095
Reflections (test)	3,371	7,569
R_{cryst} [d] / R_{free} [e] (%)	19.7/23.8	17.8/21.1
No. of atoms	4,903	5,350
Macromolecules	4,765	4,775
Glycans	28	14
Solvent	124	561
Average B-value (Å^2)	52	38
Macromolecules	52	37
Glycans	30	69
Solvent	49	41
Wilson B-value (Å^2)	45	26
RMSD from ideal geometry		
Bond length (Å)	0.007	0.018
Bond angle (°)	1.15	1.47
Ramachandran statistics (%)		
Favored	97.1	97.9
Outliers	0.16	0.00
PDB code	Pending	Pending

53   [a] Numbers in parentheses refer to the highest resolution shell.
54   [b] $R_{sym} = \Sigma_{hkl} \Sigma_i \mid I_{hkl,i} - <I_{hkl}> \mid / \Sigma_{hkl} \Sigma_i I_{hkl,i}$ and $R_{pim} = \Sigma_{hkl} (1/(n-1))^{1/2} \Sigma_i \mid I_{hkl,i} - <I_{hkl}> \mid / \Sigma_{hkl} \Sigma_i I_{hkl,i}$, where $I_{hkl,i}$ is the scaled
55   intensity of the ith measurement of reflection h, k, l, $<I_{hkl}>$ is the average intensity for that reflection, and n is the
56   redundancy.
57   [c] $CC_{1/2}$ = Pearson correlation coefficient between two random half datasets.
58   [d] $R_{cryst} = \Sigma_{hkl} \mid F_o - F_c \mid / \Sigma_{hkl} \mid F_o \mid$ x 100, where F_o and F_c are the observed and calculated structure factors, respectively.
59   [e] R_{free} was calculated as for R_{cryst}, but on a test set comprising 5% of the data excluded from refinement.
60

61 **Supplementary Table 2. Hydrogen bonds and salt bridges identified at the**
62 **antibody-RBD interface using the PISA program.**
63

COVA2-04	Distance [Å]	SARS-CoV-2 RBD
Hydrogen bonds		
H:THR28[N]	3.1	A:ALA475[O]
H:ASN32[ND2]	3.1	A:ALA475[O]
H:TYR33[OH]	2.6	A:LEU455[O]
H:SER53[N]	3.5	A:TYR421[OH]
H:SER53[OG]	3.1	A:TYR421[OH]
H:SER53[OG]	2.4	A:ARG457[O]
H:GLY54[N]	2.9	A:TYR421[OH]
H:SER56[OG]	2.3	A:ASP420[OD2]
H:ARG94[NH1]	3.1	A:ASN487[OD1]
H:ARG94[NH2]	3.2	A:ASN487[OD1]
H:ARG94[NH2]	3.7	A:TYR489[OH]
H:ARG98[NE]	3.9	A:GLN493[OE1]
H:ARG98[NH1]	3.1	A:SER494[O]
H:GLY26[O]	2.6	A:ASN487[ND2]
H:SER31[O]	2.7	A:TYR473[OH]
H:GLU97[OE1]	3.2	A:LYS417[NZ]
H:GLU97[OE2]	2.8	A:TYR453[OH]
L:TYR32[OH]	3.5	A:TYR453[OH]
L:SER31[OG]	3.6	A:TYR495[O]
L:SER29[OG]	3.8	A:GLY496[O]
L:SER27A[OG]	3.2	A:THR500[O]
L:SER29[OG]	3.7	A:ASN501[OD1]
L:SER93[OG]	2.7	A:TYR505[OH]
L:SER93[N]	3.8	A:TYR505[OH]
L:GLY92[O]	2.9	A:ARG403[NH1]
L:SER93[OG]	3.8	A:ARG403[NH1]
Salt bridges		
H:GLU97[OE1]	3.2	A:LYS417[NZ]

64
65

COVA2-39	Distance [Å]	SARS-CoV-2 RBD
Hydrogen bonds		
H:THR53[N]	3.4	A:GLU484[OE2]
H:THR53[OG1]	3.6	A:GLU484[OE2]
H:GLY54[N]	2.8	A:GLU484[OE2]
H:THR56[N]	3.3	A:GLU484[OE1]
H:THR56[OG1]	2.7	A:GLU484[OE1]
H:TYR58[OH]	2.6	A:GLU484[O]
H:GLU100C[N]	3.8	A:ASN487[OD1]
H:GLU100C[N]	2.9	A:TYR489[OH]
H:GLU100C[OE2]	3.0	A:ASN487[N]
H:GLU100C[OE2]	2.5	A:TYR489[OH]
H:SER30[O]	3.2	A:GLN493[NE2]
L:SER95[OG]	2.8	A:PHE486[N]

66